Short Communication

Phase-reassembled high-entropy fluorites for advanced thermal barrier materials

Dowon Song [a,1], Myeungwoo Ryu [a,1], Janghyeok Pyeon [b,1], Hak-Beom Jeon [c], Taeseup Song [a,], Ungyu Paik [a], Byung-il Yang [b], Yeon-Gil Jung [b,**], Yoon-Suk Oh [c]*

[a] Department of Energy Engineering, Hanyang University, Seoul 133-791, Republic of Korea
[b] Department of Materials Convergence and System Engineering, Changwon National University, Changwon, Gyeongnam 641-773, Republic of Korea
[c] Korea Institute of Ceramic Engineering and Technology, 3321 Gyeongchung Rd. Shindun-myeon, Gyeonggi-do, 17303, Republic of Korea

ARTICLE INFO

ABSTRACT

Thermal insulating materials are in high demand for heat flux regulation as they enhance energy conversion efficiency and reduce the consumption of fossil fuels. In this study, phase-reassembled high-entropy oxides (HEOs) were successfully produced via conventional solid-state reaction, and their thermophysical properties were investigated. Promising thermal barrier coating (TBC) candidates, $A_2B_2O_7$ and $A_3B'O_7$ oxides, were reassembled to a single defective fluorite structure to further reduce the thermal conductivity via an entropy-stabilization strategy. The phase-reassembled HEO ceramics exhibited low thermal conductivity (1.06 W/m·K) and glass-like thermal conduction behavior owing to their highly distorted crystal structure. In addition, their compatible thermal expansion (~9.95×10^{-6}/K) suggests that the phase-reassembled HEOs are promising candidates for new thermal barrier materials. This study proposes a new strategy for reducing the thermal conductivity via phase reassemble beyond simply increasing the number of components.

1. Introduction

Thermal insulating materials are in high demand for heat flux regulation as they enhance the energy conversion efficiency and reduce the consumption of fossil fuels. For example, there is a high demand for ceramics with low thermal conductivities in thermal barrier coatings (TBCs), which are employed in the hot components of gas turbines and aircraft engines to accommodate the higher operating temperatures that these

---

components are subjected to; in such cases, metallic substrates suffer inevitable intrinsic limitations such as poor mechanical properties and accelerated corrosion reactions [1,2]. Yttria-stabilized zirconia (YSZ) is the most commonly applied TBC material owing to its excellent thermomechanical properties, such as low thermal conductivity and high coefficient of thermal expansion (CTE) [3]. However, the application of YSZ at temperatures above 1200 °C is limited owing to its phase degradation and sintering densification, resulting in poor thermal durability and deterioration of thermal barrier performance [4,5]. Another major limitation is the relatively high thermal conductivity, which does not allow YSZ to satisfy the requirements of higher operating temperatures and enhanced thermal conversion efficiency. This has motivated the development of other materials with lower thermal conductivities.

Various materials have been proposed as alternatives to conventional YSZ, including co-doped zirconia [6—8], zirconates [9,10], and niobates [11,12]. Among them, the $A_2B_2O_7$ type rare earth zirconates ($RE_2Zr_2O_7$, RE = Y, La—Lu) exhibit a high thermal insulation performance with a thermal conductivity lower than ~2 W/m·K, which is derived from the large amount of oxygen vacancies within the fluorite-type crystal structure [13]. Moreover, they exhibit promising potential for application as thermal insulating materials at higher temperatures owing to their advantages such as high melting point and phase stability. A_3BO_7 type rare earth niobates (RE_3NbO_7, RE = La—Yb) have been reported to exhibit ultralow thermal conductivity below ~1.5 W/m·K at room temperature owing to their highly disordered fluorite structure [11].

Recently, entropy stabilization, a new strategy for engineering ceramic materials, which populates the cation sublattice with equimolar amounts of five (or more) different cations [14], has gained considerable research attention. This incorporation of cations leads to an increase in the configurational entropy and domination of the Gibbs free energy with increasing temperature, resulting in the establishment of a single phase of entropy-stabilized oxides or high-entropy oxides (HEOs). In typical ceramic materials, phonons dominate the heat conduction mechanism via phonon scattering derived from defects or distortion of the crystal structure [15,16]. In this regard, entropy stabilization can be a novel strategy for engineering materials with superior thermal insulation [17,18]. Specifically, the cation sublattice in HEOs is randomly occupied by various distinct cations that can exhibit large differences in ionic radius, bonding strength, and atomic mass, resulting in the distortion of the anion sublattice and its consequent extensive lattice scattering [18,19]. A single defective fluorite $A_2B_2O_7$ oxide, namely ($Sm_{0.2}Eu_{0.2}Tb_{0.2}Dy_{0.2}Lu_{0.2})_2Zr_2O_7$ ceramic aerogel, exhibits an ultralow thermal conductivity of ~0.0031 W/m·K at room temperature with a large thermal expansion coefficient and excellent mechanical properties [20]. Disordered defective fluorite-type A_3BO_7 niobates, namely ($Dy_{0.2}Ho_{0.2}Er_{0.2}Y_{0.2}Yb_{0.2})_3NbO_7$, have also shown ultralow thermal conductivity, suggesting their potential as a new thermal insulating material [21]. Recently, Zhang et al. reported the extremely low thermal conductivity of ($La_{0.2}Nd_{0.2}Sm_{0.2}Gd_{0.2}Yb_{0.2})_2Zr_2O_7$ ceramic foams with a pyrochlore and fluorite dual-phase structure [22].

Here, we firstly report phase-reassembled HEOs and describe their excellent thermomechanical properties for application as new thermal barrier materials. Promising TBC candidates, $A_2B_2O_7$ and $A_3B'O_7$ oxides, were reassembled in a single defective fluorite structure, namely $A_5B_2B'O_{14}$, to achieve further reduction of thermal conductivity via an entropy-stabilization strategy. These HEO materials are phase-reassembled in a single phase without forming secondary phases and changing crystal structures due to lattice distortion, even though they are composites of multiple cations. The A^{3+}, B^{4+}, and B'^{5+} cation sublattices were populated by multiple distinct cations, imposing a variety in their intrinsic properties, such as the bonding length, ionic binding strength, and mass difference. Additionally, the structural reassemble may further distort the crystal structure, enhancing the phonon lattice scattering due to the increased crystal complexity. In this study, the single-phase HEOs were synthesized via a solid-state reaction, and their highly disordered crystal structure was revealed by structural characterization. Finally, thermomechanical properties were comprehensively investigated, suggesting the promising applicability of HEOs as new TBC materials.

2. Experimental section

2.1. Material selection

The substituents for each cation site were selected based on their intrinsic properties, including the cation charge, oxide crystal structure, coordination number, and ionic radius. The cations employed at each A, B, and B' cation site have equimolar ratios among themselves. In typical $A_2B_2O_7$ oxides, the crystal structure is determined by the cation radius ratio (r_A/r_B) [23]. For 11-HEO, the A^{3+} cation sublattice was populated by the relatively smaller RE^{3+} cations, namely, Dy^{3+}, Y^{3+}, Ho^{3+}, Er^{3+}, and Yb^{3+}. In the case of 16-HEO, relatively larger RE^{3+} cations, namely La^{3+}, Nd^{3+}, Sm^{3+}, Eu^{3+}, and Gd^{3+}, were additionally incorporated into the A^{3+} cation sites to enhance the lattice distortion, which can result in larger phonon scattering and, consequently, superior thermal insulating performance. The B^{4+} and B'^{5+} cation sublattices were populated by Ti^{4+}, Zr^{4+}, Ce^{4+}, and Hf^{4+} and Nb^{5+} and Ta^{5+}, respectively, which have been reported to establish a defective fluorite structure in the space group of $Fm\text{-}3m$. Even though the difference in cationic radii of the largest and smallest ions, namely Y^{3+} and Ti^{4+}, was 50.9%, a single-phase oxide in 11- and 16-HEO was successfully achieved without the formation of any other secondary phase or impurities. The intrinsic parameters of the substitutes, namely La^{3+}, Nd^{3+}, Sm^{3+}, Eu^{3+}, Gd^{3+}, Dy^{3+}, Y^{3+}, Ho^{3+}, Er^{3+}, Yb^{3+}, Ti^{4+}, Zr^{4+}, Ce^{4+}, Hf^{4+}, Nb^{5+}, and Ta^{5+}, are listed in Table 1.

2.2. Specimen preparation

Dense 11- and 16-HEO ceramic bulks were synthesized via a conventional solid-state reaction using their stable oxides. La_2O_3, Nd_2O_3, Sm_2O_3, Eu_2O_3, Gd_2O_3, Dy_2O_3, Y_2O_3, Ho_2O_3, Er_2O_3, Yb_2O_3, Nb_2O_5, TiO_2, ZrO_2, CeO_2 (≥99% purity; Dae Jung Chemicals, Korea), HfO_2 (99%; Sigma-Aldrich, USA), and Ta_2O_5 (98%; Sigma-Aldrich, USA) were the primary oxides.

All the raw oxide powders were dried at 150 °C for 20 h to remove moisture and then precisely weighed according to

Table 1 – Oxide crystal structure, space group, coordination number (CN), ionic radius, and atomic weight of the substitutional cations.

Site	Cation	Crystal structure	Space group	CN	Ionic radius [nm]	Atomic weight
A	La^{3+}	Hexagonal	$P\text{-}62m$	8	1.16	138.9
	Nd^{3+}	Hexagonal	$P\text{-}62m$	8	1.109	144.2
	Sm^{3+}	Cubic	$Ia\text{-}3$	8	1.079	150.4
	Eu^{3+}	Cubic	$Ia\text{-}3$	8	1.066	151.9
	Gd^{3+}	Cubic	$Ia\text{-}3$	8	1.053	157.25
	Dy^{3+}	Cubic	$Ia\text{-}3$	8	1.027	162.5
	Y^{3+}	Cubic	$Ia\text{-}3$	8	1.019	88.9
	Ho^{3+}	Cubic	$Ia\text{-}3$	8	1.015	164.93
	Er^{3+}	Cubic	$Ia\text{-}3$	8	1.004	167.25
	Yb^{3+}	Cubic	$Ia\text{-}3$	8	0.985	173.04
B	Ti^{4+}	Monoclinic	$P2_1/c$	6	0.72	91.22
	Zr^{4+}	Monoclinic	$P2_1/c$	6	0.72	91.22
	Ce^{4+}	Cubic	$Fm\text{-}3m$	6	0.87	140.11
	Hf^{4+}	Monoclinic	$P2_1/c$	6	0.71	178.49
B'	Nb^{5+}	Monoclinic	$P2$	6	0.64	92.6
	Ta^{5+}	Orthorhombic	$Pmmm$	6	0.64	180.9

the desired stoichiometric ratio. The compositions of the targeted stoichiometries for 11- and 16-HEO are listed in Table 2. The oxide powders were mixed via ball milling using anhydrous alcohol and zirconia milling balls (various diameters) for 12 h at 240 rpm. The slurry mixture was dried at 120 °C for 12 h in a drying oven; the dried mixture was subsequently sieved through a 325-mesh screen to obtain a homogeneous product. Cylindrical green bodies with varying diameters for different characterization were fabricated using three steel molds via dry pressing; the samples were then densified via cold isostatic-pressing at 200 MPa for 10 min. Densified specimens were obtained after sintering at 1600 °C for 30 h.

2.3.   Characterization

The crystal structures of 11- and 16-HEO ceramics were identified using X-ray diffraction (XRD; Mini Flex II, Rigaku, Tokyo, Japan) with Cu Kα radiation (λ = 1.5418 Å) and a step size of 0.02° at a scan rate of 3°/min. The densified microstructure and chemical homogeneity were investigated via scanning electron microscopy (SEM; JSM-5610, JEOL, Tokyo, Japan) paired with an energy-dispersive spectrometer (EDS; Oxford Instruments, Oxford, UK). The crystal structure and uniform elemental distribution were further characterized via transmission electron microscopy (TEM; JEM 2100F, JEOL, Tokyo, Japan). The bulk HEO ceramics were polished to reduce the thickness to below 150 μm using diamond paper. After the dimple grinding and ion-milling processes, carbon-coated specimens were prepared for TEM observation.

A laser flash analyzer (Laser Flash Analysis, LFA 457 Micro Flash, NETZSCH, Germany) was employed in the temperature range 25—1000 °C to evaluate the thermal diffusivity (α) and specific heat capacity (C_p). The thermal conductivity values (κ') were calculated from the relationship between thermal conductivity, thermal diffusivity, heat capacity, and density (ρ), as follows:

$$\kappa' = \rho \bullet C_p \bullet \alpha \tag{1}$$

where the density was measured via Archimedes' method, and the specific heat capacity was calculated according to the Neumann−Kopp rule [24]. The effect of porosity (Φ) was considered by normalizing the thermal conductivity (κ) of the full-density solid as [25].

$$\frac{\kappa'}{\kappa} = 1 - \frac{4}{3}\Phi \tag{2}$$

Optical transmittance spectra were obtained using a diffuse reflectance UV/VIS/NIR spectrophotometer (DUV spectrophotometer; SolidSpec-3700, Shimadzu, Japan) and Fourier transform infrared spectrophotometer (FT-IR; FT/IR-4200, JASCO, Japan) for the range 1500—2500 nm and 2.5—10 μm, respectively. The bulk specimens were polished to reduce the thickness to 1 mm before measurement.

The CTEs were characterized using a high-temperature dilatometer (Dilatometer, DIL 402C, NETZSCH, Germany) in the temperature range 25—1000 °C.

The bulk modulus (B) and shear modulus (S) were measured using an oscilloscope (Tektronix, USA). Elastic modulus can be calculated using bulk modulus and shear modulus through Hooke's law. The following relationships exist between the elastic constants such as elastic modulus, shear modulus, bulk modulus, and Poisson's ratio.

$$E = 2G(1 + \upsilon) = 3B(1 - 2\upsilon) \tag{3}$$

E is the elastic modulus, B is the bulk modulus, G is the shear modulus, and υ is the Poisson ratio. The calculated elastic modulus for HEO materials is shown in Table 2.

3.   Results and discussion

3.1.   Structural characteristics

The XRD spectra of the synthesized HEOs are shown in Fig. 1(a). Both 11- and 16-HEO exhibit a single-phase structure without any impurities or secondary phases, indicating that a single defective fluorite structure is successfully prepared as

Table 2 — Fabricated 11- and 16-HEOs, along with their composition, radius differences between A-site cation, cation radius ratio (r_A/r_B), densities, average grain size, and Elastic modulus.

Composition (Formula: $A_5B_2B'O_{14}$)	A-site cation average radius (difference) [Å]	r_A/r_B	Theoretical density [g/cm³]	Relative Density [%]	Average grain size [μm]	Elastic modulus, E [GPa]
11-HEO	$(Dy_{0.2}Y_{0.2}Ho_{0.2}Er_{0.2}Yb_{0.2})_5$ $(Ti_{0.25}Zr_{0.25}Ce_{0.25}Hf_{0.25})_2(Nb_{0.5}Ta_{0.5})O_{14}$	1.01 (4.1%)	1.33	7.84	99.39	5.56 ± 1.03	172.3 ± 3.8
16-HEO	$(La_{0.1}Nd_{0.1}Sm_{0.1}Eu_{0.1}Gd_{0.1}Dy_{0.1}Y_{0.1}Ho_{0.1}Er_{0.1}Yb_{0.1})_5$ $(Ti_{0.25}Zr_{0.25}Ce_{0.25}Hf_{0.25})_2(Nb_{0.5}Ta_{0.5})O_{14}$	1.0517 (16.6%)	1.39	7.52	99.11	5.53 ± 0.89	165.8 ± 4.4

entropy-driven solid solutions in a space group of *Fm-3m* (ICSD: 60,400). The establishment of cubic defective fluorite implies that all the cations are randomly distributed regardless of the cation sites, which is similar to that in cubic fluorite YSZ, in which 1/50 of the anion sublattice is vacant owing to the dissolution of 3—4 mol% of yttria into the zirconia matrix. HEOs possess 1/8 of the empty anion sublattice in the fluorite structure to maintain the chemical balance [26,27]. The larger amounts of oxygen vacancies facilitate phonon scattering via a mass difference impurity scattering mechanism, resulting in superior thermal insulating performance. Compared to 11-HEO, the main diffraction pattern of the (111) plane of 16-HEO is slightly shifted to a lower angle owing to the relatively larger average cationic radius of the A-site substituents (Table 2).

The Raman spectra reveals the sensitive information of cation-oxygen vibrations, whereas the XRD spectra is more informative for investigating the disorder in the cation sublattice rather than the oxygen sublattice [28]. Fig. 1(b) shows the Raman spectra of 11- and 16-HEO, which determine the relative degree of local disorder in the defective fluorite structure. The cubic fluorite structure in a space group of *Fm-3m* possesses only one Raman active vibration mode in the $200-800$ cm^{-1} Raman shift [29]. However, very broad Raman spectra were obtained from both 11- and 16-HEO. This is because of their severely distorted crystal structures. The Raman peak broadening originates from the poor interpretation of the crystal symmetry, indicating a significant distortion of the oxygen sublattice. In 11- and 16-HEO, the distortion of the oxygen sublattice originates from the numerous cationic antisites that are developed by populated cation sites. Several previous reports have indicated similar broadened Raman peaks between 200 and 800 cm^{-1} in cubic fluorite structures, such as $Y_2Zr_2O_7$, $Y_2Hf_2O_7$, $Ho_2Hf_2O_7$, and $Er_2Hf_2O_7$, confirming the severe distortion of the oxygen sublattice of 11- and 16-HEO, which leads to enhanced thermal insulating performance [30].

The formation of an entropy-stabilized solid solution was further characterized by TEM observation. Fig. 1(c) and (d) show the TEM images of 11- and 16-HEO around the triple boundary, respectively. As shown in the TEM images, there are no other secondary phases around the triple boundaries (white arrows), indicating that both HEOs are constructed as monocrystal structures of solid solutions without any secondary phases or impurities. Furthermore, selected area electron diffraction (SAED) patterns were obtained to determine the crystal structure of the different grains from positions A, B, C, and D, and are displayed in the insets of Fig. 1(c) and (d), respectively. The SAED patterns taken from the [011] and [−112] directions match the fluorite structure, corresponding to the XRD spectra (Fig. 1(a)). Furthermore, the SAED patterns illustrate the excellent crystallinity and single phase of both HEOs.

To better understand the chemical homogeneity and absence of impurities or secondary phases, the typical microstructures and corresponding elemental distributions of HEOs were evaluated at different resolutions (Fig. 2). The low-magnification images in Fig. 2(a) and (b) reveal that obvious micro-voids or secondary phases around the triple junction and grain boundaries were not observed. The measured

density of HEOs and their average grain sizes are listed in Table 2, confirming that the grain size of 11-HEO is larger than that of 16-HEO, even though 11-HEO possesses a relatively larger ionic mass at the A^{3+} cation site, which restrains the atomic displacement for atomic diffusion, resulting in a decrease in the atomic diffusion coefficient [31,32]. This characteristic implies a better sintering resistance of 16-HEO, originating from the well-known sintering resistance mechanism, sluggish diffusion, which is one of the core properties of high-entropy materials [33,34]. The incorporation of multiple cations induces significant lattice distortion in the single-phase solid solution, hindering the ionic movement and their diffusion. These sintering resisting characteristics can prevent microstructural densification, avoiding the deterioration of thermal insulating performance as well as the catastrophic failure of TBCs, which can occur in densified brittle ceramic materials. The high-magnification EDS, which is obtained from the blue box area in Fig. 2(c) and (d), also confirms the chemical homogeneity of HEOs, showing the homogeneous dispersion of all elements. These results confirmed the compositional uniformity without any elemental clustering or segregation. Furthermore, no specific micro-voids or secondary phase were observed around the grain boundaries and their triple junction, implying that both HEOs were fully densified, corresponding to their measured density using the Archimedes' method.

3.2. Thermal physical properties

The experimental thermal conductivities of the HEO ceramics were obtained using Eq. (1) and were further normalized using Eq. (2), as shown in Fig. 3(a). The thermal conductivities of 11- and 16-HEO ceramics are in the range 1.27—1.56 and 1.06—1.32 W/m·K, respectively. At room temperature, the thermal conductivities of the 11- and 16-HEO ceramics are close to Clarke's minimum conductivity limit [35,36]. The form of phonon-mediated thermal conductivity (K) according to Clarke's model is as follows:

$$K = \frac{1}{3}cvl \qquad (3)$$

Where c is the heat capacity per unit volume, v is the average speed of collective lattice vibration, and l is the average phonon mean free path value. Also, according to the Clarke
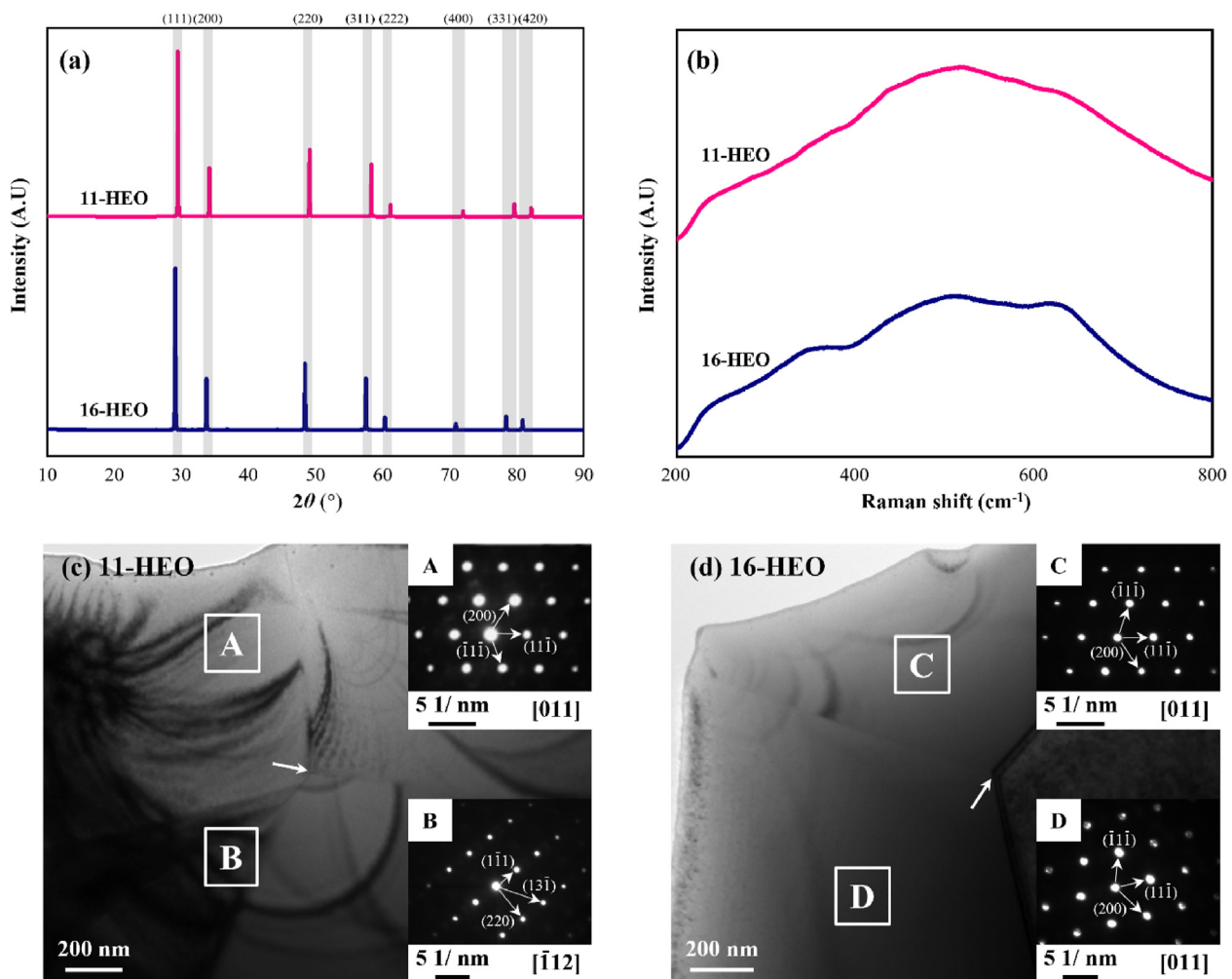
Fig. 1 — Structural characterization of HEO ceramics, namely (a) XRD patterns, (b) Raman spectrum, and (c) and (d) TEM images of 11- and 16-HEO, respectively. The insets in (c) and (d) show SAED patterns obtained from positions A, B, C, and D, respectively. The white arrows indicate the triple boundary.
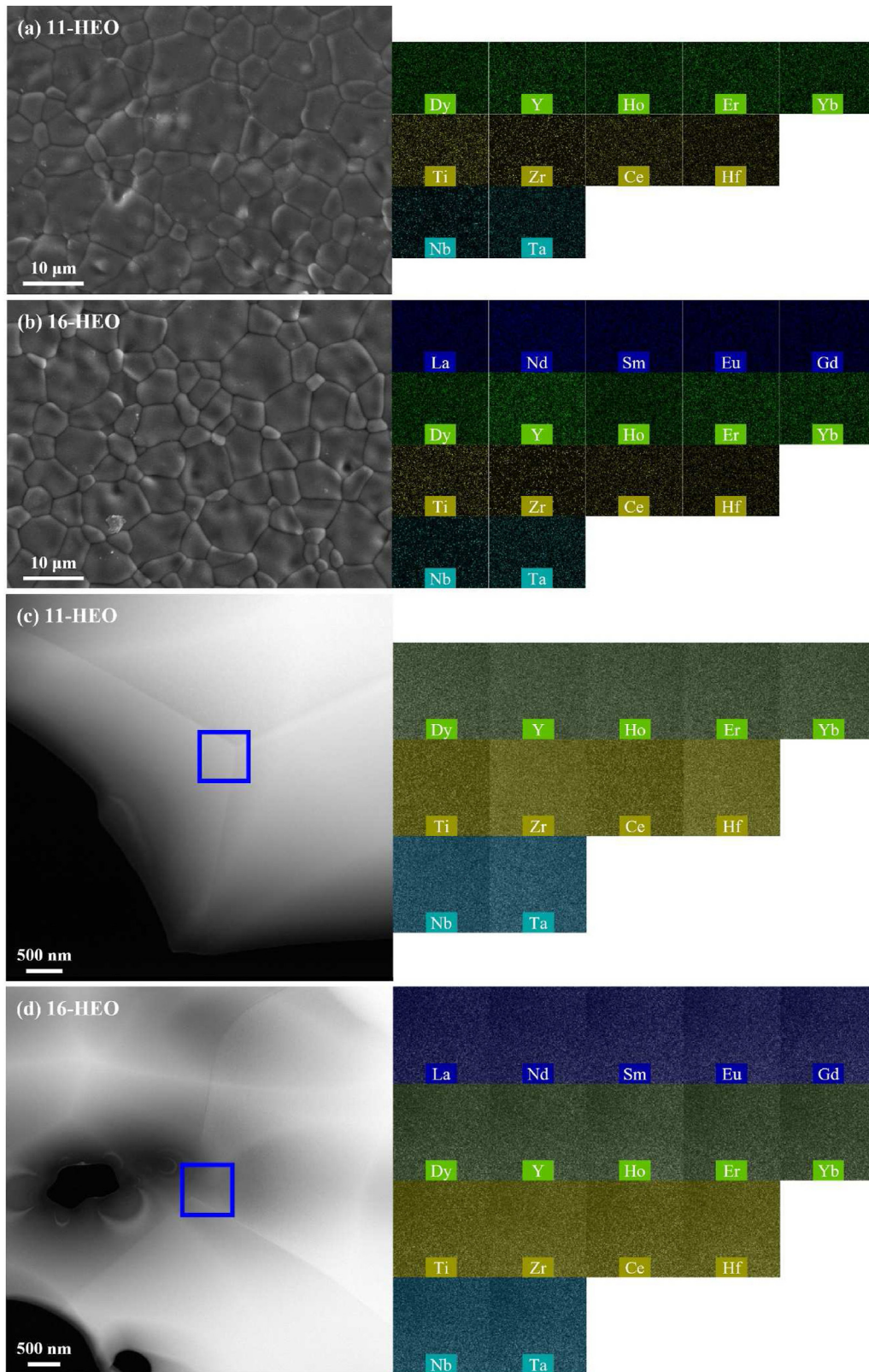
Fig. 2 — Microstructure and elemental distribution of HEO ceramics obtained using (a), (b) SEM, and (c), (d) TEM.
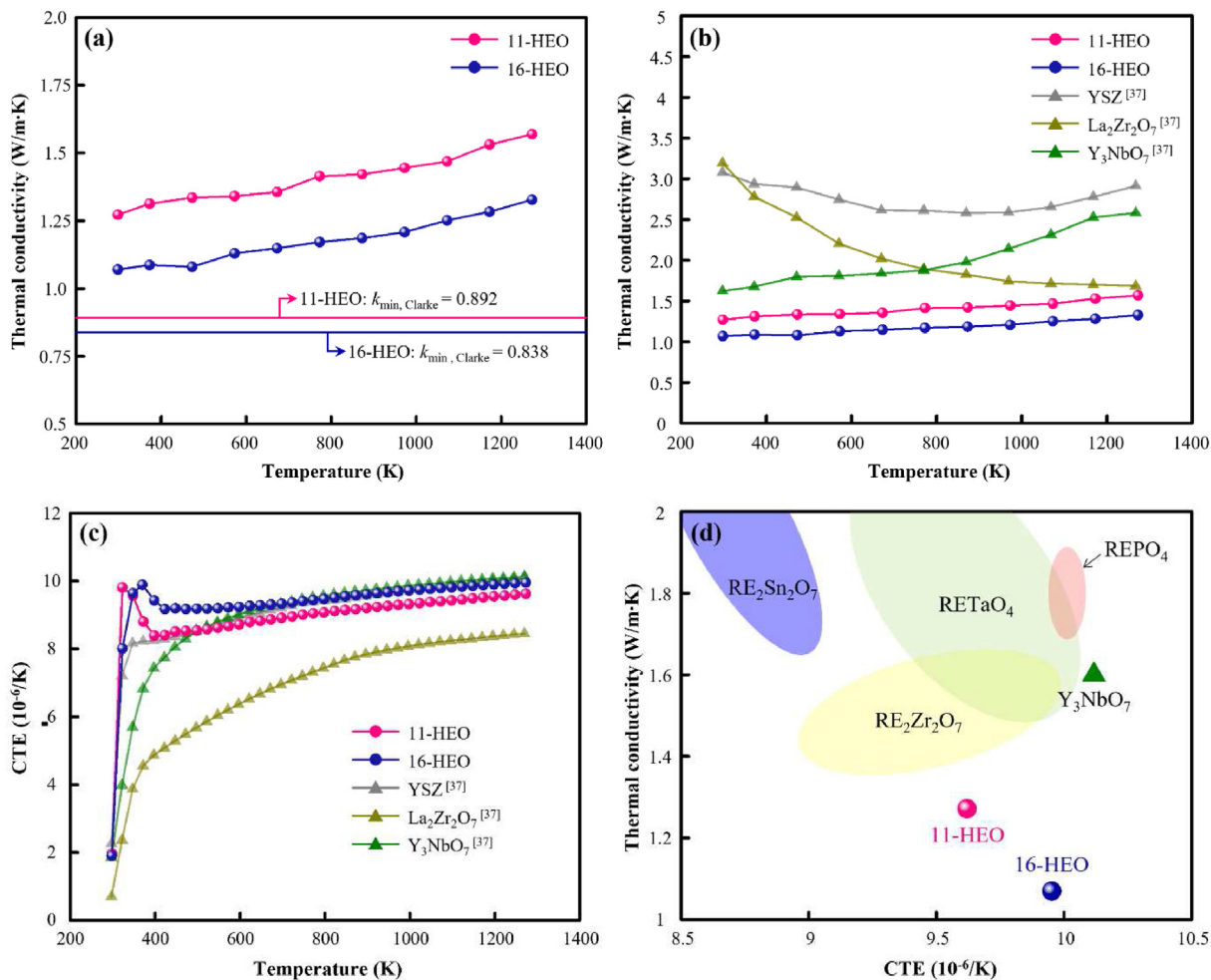
Fig. 3 − **Thermal physical properties of HEO ceramics. (a) Experimental and minimum thermal conductivity, (b) thermal conductivity comparison, (c) thermal expansion coefficient, and (d) thermal conductivity as a function of thermal expansion coefficient.**

models in the case of glass-like, the minimum thermal conductivity can be thought of as the $l \to a$ (a is the interatomic spacing). Since synthesized the HEO materials have a glass-like disorder degree, we substituted it as a value of an instead of l, resulting in a calculated minimum thermal conductivity of 0.892 W/m·K for 11-HEO and 0.838 W/m·K for 16-HEO. When comparing the calculated value and the thermal conductivity measured at room temperature, it was found that 11-HEO was about 43% higher and 16-HEO was 26% higher than the calculated thermal conductivity. Both HEOs show a slightly increasing tendency in thermal conduction behavior with increasing temperature, similar to glass-like polycrystalline materials. As shown in Fig. 3(b), the thermal conductivities of 11- and 16-HEO ceramics are less than half of that of YSZ (3.06 W/m·K) [37]. Furthermore, the thermal insulating performance of phase-reassembled HEOs is superior to that of their primitive oxides, $La_2Zr_2O_7$ (LZO) and Y_3NbO_7 (YNO), which are the representative TBC candidates of $A_2B_2O_7$ and $A_3B'O_7$ oxides [37]. The amorphous-like ultralow thermal conductivities of 11- and 16-HEO originate from their highly disordered ceramic materials [11,38−40]. Single-phase HEOs were established because of their high configurational

entropy; their cation sites were populated by multiple distinct cations with large differences in ionic radii of up to 46.4% and 57.8% for 11- and 16-HEO, respectively. To accommodate the population of multiple cations, the anion sublattice gets significantly distorted, as confirmed by Raman analysis (Fig. 1(b)). Compared to YSZ, the superior thermal insulating performance originates from the larger oxygen vacancies, where 1/8 of the anion sites are vacant in HEOs, whereas YSZ possesses only 1/50 empty anion sites [19]. Furthermore, the multiple cations and oxygen vacancies in HEOs were randomly distributed within the defective fluorite structure as a single-phase solid solution, whereas La^{3+}, Zr^{4+}, and oxygen vacancies in LZO were located at specific sites as intermetallic compounds [41,42]. Consequently, these structural characteristics of HEOs generate significant structural distortion and random distribution of multiple cations and oxygen vacancies, resulting in a constant phonon mean free path similar to that of an amorphous material [43].

For TBC materials, the CTE must be compatible with that of metallic bond coat materials ($13−16 \times 10^{-6}$/K) to minimize CTE mismatch and reduce the thermomechanical stress at the interface [44]. It is known that single $A_2B_2O_7$ type oxides with a

pyrochlore or fluorite structure show limited ability to replace conventional YSZ owing to their low CTE. The 11- and 16-HEO exhibited larger CTEs (9.61×10^{-6}/K and 9.95×10^{-6}/K for 11- and 16-HEO at 1273 K, respectively) than the primitive $A_2B_2O_7$ oxide, LZO (8.42×10^{-6}/K at 1273 K). The CTE of 16-HEO is compatible with YSZ and YNO (10.09×10^{-6}/K and 10.11×10^{-6}/K at 1273 K), suggesting that this phase reassemble of HEO with highly disordered structure can compensate for the low CTE of primitive oxide, LZO, via evident cocktail effects, which is one of the common characteristics of high-entropy compounds [20,45,46]. The cocktail effects refer to the effect of obtaining new physical properties that do not appear in independent components when many elements are mixed, and these properties can change according to the composition variation. By contrast, it is known that CTE of ionic solids is inversely proportional to its ionic bonding strength, which can be determined by the crystal lattice energy [47]. The elastic modulus of an ionic solid material is dominated by the lattice energy, which indicates that a smaller lattice energy leads to a smaller elastic modulus [48,49]. The elastic modulus values of HEOs were obtained by; thus, it can be considered that the competitive CTE values of HEOs originated from their relatively smaller elastic modulus (172.3 ± 3.8 and 165.8 ± 4.4 GPa for 11- and 16-HEO, respectively) compared to that of conventional YSZ (223.0 ± 7.4 GPa).

Compared with many other rare earth oxide compounds for TBC materials, including their primitive oxides, such as $RE_2Zr_2O_7$ [5,50,51], $RETaO_4$ [52], $REPO_4$ [53], $RE_2Sn_2O_7$ [54], and YNO [37], the phase-reassembled HEOs show a low thermal conductivity and compatible CTE, implying that HEOs can be applied as new promising TBC materials.

4. Conclusions

Phase-reassembled HEOs were successfully synthesized via a solid-state reaction, and their thermophysical properties were investigated. Promising thermal barrier coating (TBC) candidates, $A_2B_2O_7$ and $A_3B'O_7$ oxides, were reassembled to a single defective fluorite structure, and showed glass-like ultralow thermal conductivity (1.06 W/m·K), which is superior to that of their primitive oxides, LZO and YNO. In addition, the compatible thermal expansion (~9.95×10^{-6}/K) suggests that the phase-reassembled HEOs exhibit promising applicability as new TBC materials. This study proposes a new strategy to further reduce the thermal conductivity via phase reassemble beyond simply increasing the number of components and expanding the diversity of TBC materials. Also, HEO materials are possible to make TBCs by APS and EB-PVD methods. Therefore, we plan to conduct thermal durability analysis such as thermal shock on HEO materials through follow-up studies.

Declaration of competing interest

The authors declare that they have no known competing financial interests or personal relationships that could have appeared to influence the work reported in this paper.

REFERENCES

[1] Padture NP. Advanced structural ceramics in aerospace propulsion. Nat Mater 2016;15:804–9. https://doi.org/10.1038/nmat4687.

[2] Darolia R. Thermal barrier coatings technology: critical review, progress update, remaining challenges and prospects. Int Mater Rev 2013;58:315–48. https://doi.org/10.1179/1743280413y.0000000019.

[3] Smialek JL, Miller RA. Revisiting the birth of 7YSZ thermal barrier coatings: stephan Stecura. Coatings 2018;8:255. https://doi.org/10.3390/coatings8070255.

[4] Miller RA, Smialek JL, Garlick RG. Phase stability in plasma-sprayed, partially stabilized zirconia-yttria. 1981.

[5] Vassen R, Cao X, Tietz F, Basu D, Stöver D. Zirconates as new materials for thermal barrier coatings. J Am Ceram Soc 2000;83:2023–8. https://doi.org/10.1111/j.1151-2916.2000.tb01506.x.

[6] Matsumoto M, Aoyama K, Matsubara H, Takayama K, Banno T, Kagiya Y, et al. Thermal conductivity and phase stability of plasma sprayed ZrO2–Y2O3–La2O3 coatings. Surf Coating Technol 2005;194:31–5. https://doi.org/10.1016/j.surfcoat.2004.04.078.

[7] Ma W, Mack D, Malzbender J, Vaßen R, Stöver D. Yb2O3 and Gd2O3 doped strontium zirconate for thermal barrier coatings. J Eur Ceram Soc 2008;28:3071–81. https://doi.org/10.1016/j.jeurceramsoc.2008.05.013.

[8] Wang J, Chong X, Zhou R, Feng J. Microstructure and thermal properties of RETaO4 (RE= Nd, Eu, Gd, Dy, Er, Yb, Lu) as promising thermal barrier coating materials. Scripta Mater 2017;126:24–8. https://doi.org/10.1016/j.scriptamat.2016.08.019.

[9] Mahade S, Curry N, Björklund S, Markocsan N, Nylén P, Vaßen R. Erosion performance of gadolinium zirconate-based thermal barrier coatings processed by suspension plasma spray. J Therm Spray Technol 2017;26:108–15. https://doi.org/10.1007/s11666-016-0479-4.

[10] Wan C, Zhang W, Wang Y, Qu Z, Du A, Wu R, et al. Glass-like thermal conductivity in ytterbium-doped lanthanum zirconate pyrochlore. Acta Mater 2010;58:6166–72. https://doi.org/10.1016/j.actamat.2010.07.035.

[11] Yang J, Qian X, Pan W, Yang R, Li Z, Han Y, et al. Diffused lattice vibration and ultralow thermal conductivity in the binary Ln–Nb–O oxide System. Adv Mater 2019;31:1808222. https://doi.org/10.1002/adma.201808222.

[12] Chen L, Guo J, Zhu Y, Hu M, Feng J. Features of crystal structures and thermo-mechanical properties of weberites RE3NbO7 (RE= La, Nd, Sm, Eu, Gd) ceramics. J Am Ceram Soc 2021;104:404–12. https://doi.org/10.1111/jace.17437.

[13] Wu J, Wei X, Padture NP, Klemens PG, Gell M, García E, et al. Low-thermal-conductivity rare-earth zirconates for potential thermal-barrier-coating applications. J Am Ceram Soc

2002;85:3031–5. https://doi.org/10.1111/j.1151-2916.2002.tb00574.x.

[14] Rost CM, Sachet E, Borman T, Moballegh A, Dickey EC, Hou D, et al. Entropy-stabilized oxides. Nat Commun 2015;6:1–8. https://doi.org/10.1038/ncomms9485.

[15] Callaway J. Model for lattice thermal conductivity at low temperatures. Phys Rev 1959;113:1046. https://doi.org/10.1103/PhysRev.113.1046.

[16] Xie G, Shen Y, Wei X, Yang L, Xiao H, Zhong J, et al. A bond-order theory on the phonon scattering by vacancies in two-dimensional materials. Sci Rep 2014;4:5085. https://doi.org/10.1038/srep05085.

[17] Zhang R-Z, Reece MJ. Review of high entropy ceramics: design, synthesis, structure and properties. J Mater Chem 2019;7:22148–62. https://doi.org/10.1039/C9TA05698J.

[18] Oses C, Toher C, Curtarolo S. High-entropy ceramics. Nat Rev Mater 2020;5:295–309. https://doi.org/10.1038/s41578-019-0170-8.

[19] Song D, Song T, Paik U, Lyu G, Jung Y-G, Jeon H-B, et al. Glass-like thermal conductivity in mass-disordered high-entropy (Y, Yb) 2 (Ti, Zr, Hf) 2O7 for thermal barrier material. Mater Des 2021;210:110059. https://doi.org/10.1016/j.matdes.2021.110059.

[20] Ren K, Wang Q, Shao G, Zhao X, Wang Y. Multicomponent high-entropy zirconates with comprehensive properties for advanced thermal barrier coating. Scripta Mater 2020;178:382–6. https://doi.org/10.1016/j.scriptamat.2019.12.006.

[21] Cong L, Li W, Wang J, Gu S. High-entropy (Y0. 2Gd0. 2Dy0. 2Er0. 2Yb0. 2)2Hf2O7 ceramic: a promising thermal barrier coating material. J Mater Sci Technol 2022;101:199–204. https://doi.org/10.1016/j.jmst.2021.05.054.

[22] Zhu J, Meng X, Zhang P, Li Z, Xu J, Reece MJ, et al. Dual-phase rare-earth-zirconate high-entropy ceramics with glass-like thermal conductivity. J Eur Ceram Soc 2021;41:2861–9. https://doi.org/10.1016/j.jeurceramsoc.2020.11.047.

[23] Subramanian M, Aravamudan G, Rao GS. Oxide pyrochlores—a review. Prog Solid State Chem 1983;15:55–143. https://doi.org/10.1016/0079-6786(83)90001-8.

[24] Leitner J, Chuchvalec P, Sedmidubský D, Strejc A, Abrman P. Estimation of heat capacities of solid mixed oxides. Thermochim Acta 2002;395:27–46. https://doi.org/10.1016/S0040-6031(02)00177-6.

[25] Schlichting K, Padture N, Klemens P. Thermal conductivity of dense and porous yttria-stabilized zirconia. J Mater Sci 2001;36:3003–10. https://doi.org/10.1023/A:1017970924312.

[26] Cleave AR. Atomic scale simulations for waste form applications. UK: University of London London; 2006.

[27] Zhao M, Pan W, Wan C, Qu Z, Li Z, Yang J. Defect engineering in development of low thermal conductivity materials: a review. J Eur Ceram Soc 2017;37:1–13. https://doi.org/10.1016/j.jeurceramsoc.2016.07.036.

[28] Glerup M, Nielsen OF, Poulsen FW. The structural transformation from the pyrochlore structure, A2B2O7, to the fluorite structure, AO2, studied by Raman spectroscopy and defect chemistry modeling. J Solid State Chem 2001;160:25–32. https://doi.org/10.1006/jssc.2000.9142.

[29] Mandal B, Krishna P, Tyagi A. Order–disorder transition in the Nd2− yYyZr2O7 system: probed by X-ray diffraction and Raman spectroscopy. J Solid State Chem 2010;183:41–5. https://doi.org/10.1016/j.jssc.2009.10.010.

[30] Mandal B, Garg N, Sharma SM, Tyagi A. Preparation, XRD and Raman spectroscopic studies on new compounds RE2Hf2O7 (RE= Dy, Ho, Er, Tm, Lu, Y): pyrochlores or defect-fluorite? J Solid State Chem 2006;179:1990–4. https://doi.org/10.1016/j.jssc.2006.03.036.

[31] Uhlenbeck GE, Ornstein LS. On the theory of the Brownian motion. Phys Rev 1930;36:823. https://doi.org/10.1103/PhysRev.36.823.

[32] Che J, Wang X, Liu X, Liang G, Zhang S. Outstanding sintering resistance in pyrochlore-type La2 (Zr0. 7Ce0. 3) 2O7 for thermal barrier coatings material. Ceram Int 2021;47:6996–7004. https://doi.org/10.1016/j.ceramint.2020.11.050.

[33] Djenadic R, Sarkar A, Clemens O, Loho C, Botros M, Chakravadhanula VS, et al. Multicomponent equiatomic rare earth oxides. Materials Research Letters 2017;5:102–9. https://doi.org/10.1080/21663831.2016.1220433.

[34] Grzesik Z, Smoła G, Stygar M, Dąbrowa J, Zajusz M, Mroczka K, et al. Defect structure and transport properties in (Co, Cu, Mg, Ni, Zn) O high entropy oxide. J Eur Ceram Soc 2019;39:4292–8. https://doi.org/10.1016/j.jeurceramsoc.2019.06.018.

[35] Agne MT, Hanus R, Snyder GJ. Minimum thermal conductivity in the context of diffuson-mediated thermal transport. Energy Environ Sci 2018;11:609–16. https://doi.org/10.1039/C7EE03256K.

[36] Clarke DR. Materials selection guidelines for low thermal conductivity thermal barrier coatings. Surf Coating Technol 2003;163:67–74. https://doi.org/10.1016/S0257-8972(02)00593-5.

[37] Song D, Kim J, Lyu G, Pyeon J, Jeon H-B, Oh Y-S, Song T, et al. Effect of cation substitution on thermophysical properties of fluorite A3BO7 ceramics. J Alloys Compd 2021;883:160848. https://doi.org/10.1016/j.jallcom.2021.160848.

[38] Chen L, Jiang Y, Chong X, Feng J. Synthesis and thermophysical properties of RETa3O9 (RE= Ce, Nd, Sm, Eu, Gd, Dy, Er) as promising thermal barrier coatings. J Am Ceram Soc 2018;101:1266–78. https://doi.org/10.1111/jace.15268.

[39] Chen L, Hu M, Wu F, Song P, Feng J. Thermo-mechanical properties of fluorite Yb3TaO7 and Yb3NbO7 ceramics with glass-like thermal conductivity. J Alloys Compd 2019;788:1231–9. https://doi.org/10.1016/j.jallcom.2019.02.317.

[40] Karabaş M. Production and characterization of Nd and Dy doped lanthanum zirconate-based thermal barrier coatings. Surf Coating Technol 2020;394:125864. https://doi.org/10.1016/j.surfcoat.2020.125864.

[41] Sickafus K, Minervini L, Grimes R, Valdez J, Ishimaru M, Li F, et al. Radiation tolerance of complex oxides. Science 2000;289:748–51. https://doi.org/10.1126/science.289.5480.748.

[42] Lumpkin GR, Pruneda M, Rios S, Smith KL, Trachenko K, Whittle KR, et al. Nature of the chemical bond and prediction of radiation tolerance in pyrochlore and defect fluorite compounds. J Solid State Chem 2007;180:1512–8. https://doi.org/10.1016/j.jssc.2007.01.028.

[43] Braun JL, Rost CM, Lim M, Giri A, Olson DH, Kotsonis GN, et al. Charge-induced disorder controls the thermal conductivity of entropy-stabilized oxides. Adv Mater 2018;30:1805004. https://doi.org/10.1002/adma.201805004.

[44] Liu B, Liu Y, Zhu C, Xiang H, Chen H, Sun L, et al. Advances on strategies for searching for next generation thermal barrier coating materials. J Mater Sci Technol 2019;35:833–51. https://doi.org/10.1016/j.jmst.2018.11.016.

[45] Yeh J-W. Alloy design strategies and future trends in high-entropy alloys. JOM (J Occup Med) 2013;65:1759–71. https://doi.org/10.1007/s11837-013-0761-6.

[46] Senkov ON, Wilks G, Scott J, Miracle DB. Mechanical properties of Nb25Mo25Ta25W25 and V20Nb20Mo20Ta20W20 refractory high entropy alloys. Intermetallics 2011;19:698–706. https://doi.org/10.1016/j.intermet.2011.01.004.

[47] Barsoum MW. Fundamentals of ceramics. CRC press; 2019.

[48] Bengisu M. Properties of ceramic materials and their evaluation, Engineering Ceramics. Springer; 2001. p. 209—362. https://doi.org/10.1007/978-3-662-04350-9_4.

[49] Wu F, Wu P, Zhou Y, Chong X, Feng J. The thermo-mechanical properties and ferroelastic phase transition of RENbO4 (RE= Y, La, Nd, Sm, Gd, Dy, Yb) ceramics. J Am Ceram Soc 2020;103:2727—40. https://doi.org/10.1111/jace.16926.

[50] Feng J, Xiao B, Wan C, Qu Z, Huang Z, Chen J, et al. Electronic structure, mechanical properties and thermal conductivity of Ln2Zr2O7 (Ln= La, Pr, Nd, Sm, Eu and Gd) pyrochlore. Acta Mater 2011;59:1742—60. https://doi.org/10.1016/j.actamat.2010.11.041.

[51] Schelling‖ P, Phillpot¶ S, Grimes R. Optimum pyrochlore compositions for low thermal conductivity. Phil Mag Lett 2004;84:127—37. https://doi.org/10.1080/09500830310001646699.

[52] Chen L, Hu M, Wu P, Feng J. Thermal expansion performance and intrinsic lattice thermal conductivity of ferroelastic RETaO4 ceramics. J Am Ceram Soc 2019;102:4809—21. https://doi.org/10.1111/jace.16328.

[53] Pan W. New class of refractory ceramics for thermal barrier coatings. 2014.

[54] Feng J, Xiao B, Zhou R, Pan W. Thermal expansion and conductivity of RE2Sn2O7 (RE= La, Nd, Sm, Gd, Er and Yb) pyrochlores. Scripta Mater 2013;69:401—4. https://doi.org/10.1016/j.scriptamat.2013.05.030.